ADVANCED FUNCTIONAL MATERIALS
www.afm-journal.de

Correlating Nanocrystalline Structure with Electronic Properties in 2D Platinum Diselenide

*Sebastian Lukas, Oliver Hartwig, Maximilian Prechtl, Giovanna Capraro, Jens Bolten, Alexander Meledin, Joachim Mayer, Daniel Neumaier, Satender Kataria, Georg S. Duesberg, and Max C. Lemme**

Platinum diselenide ($PtSe_2$) is a 2D material with outstanding electronic and piezoresistive properties. The material can be grown at low temperatures in a scalable manner, which makes it extremely appealing for many potential electronics, photonics, and sensing applications. Here, the nanocrystalline structure of different $PtSe_2$ thin films grown by thermally assisted conversion (TAC) is investigated and is correlated with their electronic and piezoresistive properties. Scanning transmission electron microscopy for structural analysis, X-ray photoelectron spectroscopy (XPS) for chemical analysis, and Raman spectroscopy for phase identification are used. Electronic devices are fabricated using transferred $PtSe_2$ films for electrical characterization and piezoresistive gauge factor measurements. The variations of crystallite size and their orientations are found to have a strong correlation with the electronic and piezoresistive properties of the films, especially the sheet resistivity and the effective charge carrier mobility. The findings may pave the way for tuning and optimizing the properties of TAC-grown $PtSe_2$ toward numerous applications.

1. Introduction

Layered platinum diselenide ($PtSe_2$) is a transition metal dichalcogenide (TMDC) with promising properties for novel electronic and sensing devices.[1–6] It can be sub-classified among the 2D materials as a noble metal dichalcogenide (NMDC). It is a semiconductor with a bandgap of up to 1.6 eV in monolayer form and becomes a semimetal as the number of layers increases.[7–10] This metal-semiconductor transition may be utilized in lateral heterostructures with low-ohmic contacts of the semimetal phase to a channel of semiconducting $PtSe_2$ for electronics applications.[11–13] The predicted phonon-limited room-temperature charge carrier mobility of $PtSe_2$ is higher than 1000 $cm^2\ V^{-1}\ s^{-1}$ [14] with the highest experimentally measured value of 625 $cm^2\ V^{-1}\ s^{-1}$.[15] Furthermore, $PtSe_2$ films have been grown as both p-type and n-type semiconductors by varying the growth parameters,[16] which could pave the way for $PtSe_2$-based CMOS circuits. The semi-metallic nature of few-layer $PtSe_2$ suggests applications in infrared photodetection.[1,3,17,18] Finally, $PtSe_2$ has been demonstrated as material for highly sensitive membrane-based pressure sensors due to its high negative piezoresistive gauge factor (GF) of up to –84,[2] which is attributed to a change of the bandgap under mechanical strain.[19] The piezoresistive effect may be exploited in membrane-based nanoelectromechanical systems, with high potential for pressure, strain, acceleration or other sensors.[20]

S. Lukas, G. Capraro, Dr. S. Kataria, Prof. M. C. Lemme
Chair of Electronic Devices
RWTH Aachen University
Otto-Blumenthal-Str. 2, 52074 Aachen, Germany
E-mail: max.lemme@eld.rwth-aachen.de

O. Hartwig, M. Prechtl, Prof. G. S. Duesberg
Institute of Physics
Faculty of Electrical Engineering and Information Technology (EIT 2)
Universität der Bundeswehr München
Werner-Heisenberg-Weg 39, 85577 Neubiberg, Germany

The ORCID identification number(s) for the author(s) of this article can be found under https://doi.org/10.1002/adfm.202102929.

DOI: 10.1002/adfm.202102929

G. Capraro, Dr. J. Bolten, Prof. D. Neumaier, Prof. M. C. Lemme
AMO GmbH
Advanced Microelectronic Center Aachen
Otto-Blumenthal-Str. 25, 52074 Aachen, Germany

Dr. A. Meledin, Prof. J. Mayer
Central Facility for Electron Microscopy
RWTH Aachen University
Ahornstr. 55, 52074 Aachen, Germany

Dr. A. Meledin, Prof. J. Mayer
Ernst Ruska-Centre for Microscopy and Spectroscopy with Electrons (ER-C)
Forschungszentrum Jülich GmbH
52425 Jülich, Germany

Prof. D. Neumaier
Chair of Smart Sensor Systems
Bergische Universität Wuppertal
Lise-Meitner-Str. 13, 42119 Wuppertal, Germany

Table 1. Overview of the experimental results from the samples studied within this work. $R_{\square,4P}$ and $R_{\square,TLM}$ are the sheet resistance values determined from four-point and TLM measurements, respectively. R_c is the contact resistance determined from TLM measurements. μ_F and μ_H are the effective charge carrier mobility values determined from four-point and Hall measurements, respectively. $n_\square$ is the sheet carrier concentration extracted from Hall measurements. E_A is the activation energy extracted from high temperature measurements of the device resistance without gate bias. GF is the piezoresistive gauge factor. E_g FWHM is the width of the E_g peak determined in Raman spectroscopy. – denotes that the data was not available, * denotes that the thickness was determined from AFM measurements, and • denotes that the thickness was estimated from the TEM images; other thicknesses are estimated from the initial Pt thicknesses.

Material batch	Growth substrate	Symbol	Sample number	Approx. thickness [nm]	$R_{\square,4P}$ [kΩ □$^{-1}$]	$R_{\square,TLM}$ [kΩ □$^{-1}$]	R_c [kΩ µm]	μ_F [cm^2 V^{-1} s^{-1}]	μ_H [cm^2 V^{-1} s^{-1}]	$n_\square$ [cm^{-2}]	E_A [meV]	GF	E_g FWHM [cm^{-1}]
1	Si/SiO_2	★	1	5•	8.3	6.3	1.7	13.2	5.4	2.1×10^{14}	≤ 5	−26.8	4.83
2	quartz	●	2A	5•	748 000	50 000	32 000	0.0036	–	–	160	13.5	7.54
		●	2B	5	667 000	160 000	–	0.0023	–	–	134	–	7.09
		●	2C	7.5	–	–	–	–	–	–	–	–	–
		●	2D	15•	20.1	16.0	1.3	1.5	–	–	22	4.4	5.07
3	quartz	⬟	3	15•	10.8	10.5	0.97	3.9	2.1	2.9×10^{14}	15	−7.3	5.11
4	Si/SiO_2	◆	4A	7.6*	50.7	71.1	–	2.7	15.3	7.3×10^{12}	32	−64.9	5.12
		◆	4B	13.7*	6.0	6.1	2.1	3.1	4.9	2.3×10^{14}	13	−33.9	4.71
		◆	4C	22.3*	2.6	2.9	0.7	3.3	–	–	15	6.6	4.32

In addition to the high application potential, $PtSe_2$ exhibits long-term stability in air[21] and it can be grown at complementary metal oxide semiconductor (CMOS)-back end of line (BEOL)-compatible temperatures (≤450 °C),[1,22] through thermally assisted conversion (TAC) of thin platinum films. Furthermore, TAC allows wafer-scale growth on various substrates, such as silicon dioxide (SiO_2),[15,22–25] aluminum oxide (Al_2O_3),[11] and other rigid substrates,[26] but also on flexible substrates.[15,27]

Even though the application potential of $PtSe_2$ has been clearly demonstrated, literature data of electronic properties shows high variability. Most studies report mobilities lower than 50 cm^2 V^{-1} s^{-1} [11,16,25,28–31] with some lower than 1 cm^2 V^{-1} s^{-1} [12,23,32] for TAC-grown $PtSe_2$. Also, semiconducting behavior has been reported for much thicker films than the theoretically expected mono- and bilayers.[25] The p- and n-doping of $PtSe_2$ films is reported to depend on the selenization process.[16] Further we have also found significant variations in the piezoresistive gauge factor in our earlier report.[27] Thus, $PtSe_2$ and its electronic properties appear to be highly tunable.

TAC-grown 2D materials are mostly polycrystalline materials with thicknesses of only few atomic layers and domains in the nanometer scale.[1,8,27,33,34] Similar to other 2D materials such as graphene[35,36] or MoS_2,[37,38] the resistivity and the effective mobility are influenced by the sizes of individual crystallites and their respective orientation. Horizontally aligned layers for very thin TAC-grown films have repeatedly been reported, while thicker films have shown to possess vertically aligned layers on the substrates.[39,40] Thus, correlating the individually reported basic material properties with electronic performance in a systematic way remains challenging.

Here, we present a detailed study of $PtSe_2$ films grown by TAC at 450 °C and find a strong correlation between their microstructures and measured electronic and piezoresistive properties. Cross-sectional annular bright field and annular dark field scanning transmission electron microscopy (ABF/ADF STEM) is utilized for a thorough analysis of their microstructures. Detailed Raman analysis reveals that the peak width of the E_g mode is a suitable indicator for the film quality. Furthermore, X-ray photoelectron spectroscopy (XPS) is used for chemical analysis. Finally, we measure and analyze the electronic properties and the piezoresistive gauge factor (GF) on devices with transferred $PtSe_2$ films. We then discuss the structural composition and variations in the nanocrystalline films and present a model correlating the polycrystalline electrical resistivity and its change with temperature.[41,42]

2. Results and Discussion

$PtSe_2$ films of different thicknesses have been grown on silicon (Si)/SiO_2 and quartz substrates by TAC in different deposition chambers and in four different batches (see **Table 1** for an overview). For electronic device fabrication, the films of sample batches 1, 2, and 3 have been wet-transferred from their growth substrates onto highly p-doped (p+) Si/90 nm SiO_2 substrates. The films of sample batch 4 had been directly grown on p+ Si/90 nm SiO_2 substrates and electronic device fabrication and characterization was therefore done on the growth substrate without transfer. To verify that the transfer did not significantly modify the films, some characterization was also done on transferred films of batch 4. Films of all batches have additionally been transferred onto flexible polyimide foil (Kapton) substrates for strain gauge fabrication. Details on the material synthesis and transfer processes can be found in the experimental section.

2.1. Material Analysis

All samples were characterized using Raman spectroscopy, which provides information on their phase formation and crystallinity. The recorded spectra show the characteristic peaks of layered $PtSe_2$ at ≈ 175 cm^{-1} (E_g peak) and ≈ 205 cm^{-1} (A_{1g} peak)[8] in all examined samples (**Figure 1**a). The E_g peak positions shift to lower wave numbers for increasing film thicknesses (Figure 1b, bottom), in agreement with previous findings.[3,8,9,13,33,43,44] The shifts of the A_{1g} peak positions, however, do not display

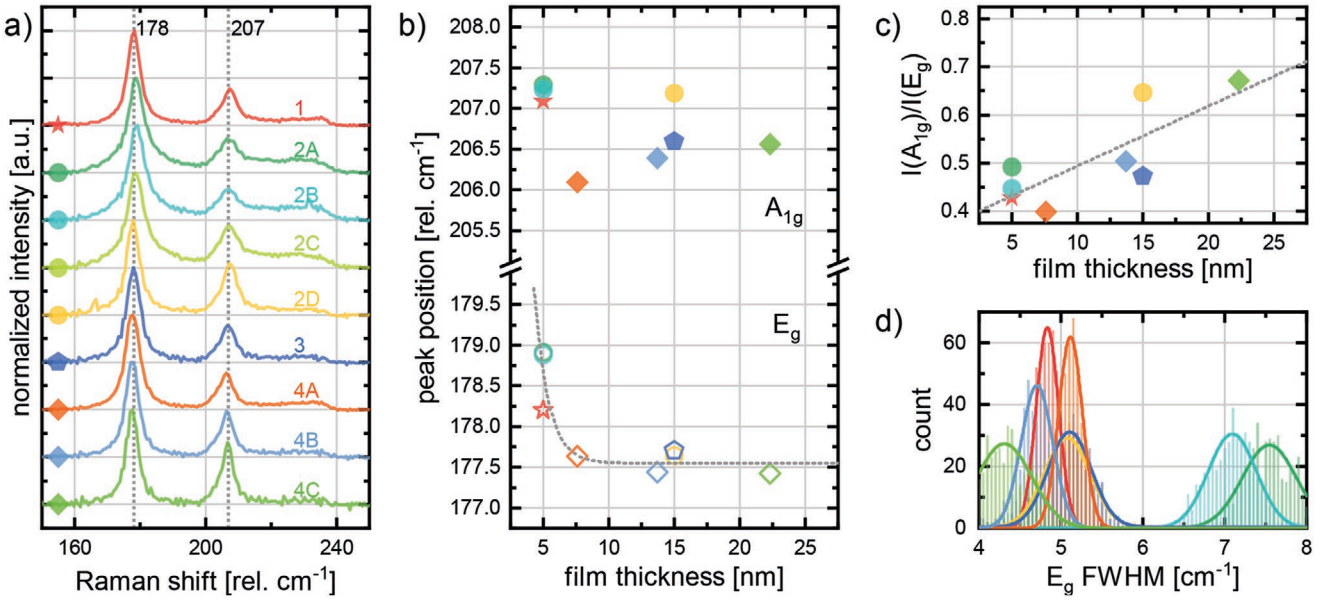

Figure 1. Raman analysis of the various $PtSe_2$ films. a) Raman spectra of nine of the examined $PtSe_2$ samples. The spectra were recorded with an integration time of 8 s and averaged over 10 accumulations. The data was then normalized to the maximum intensity of the E_g peak. For better comparison, two dotted reference lines at 178 and 207 cm^{-1} are shown. b) Shift of the E_g peak (hollow symbols) and A_{1g} peak (solid symbols) position depending on the $PtSe_2$ film thickness. c) Intensity ratio of the two characteristic Raman peaks of $PtSe_2$ over the approximate film thickness. d) Histograms of the E_g peak FWHM from Raman area scans. In all panels, the dotted lines are just a guide to the eye. Sample numbers are indicated in panel (a) and in Table 1.

an obvious dependence on the film thickness (Figure 1b, top). Furthermore, the intensity ratio of the two peaks, $I(A_{1g})/I(E_g)$, generally increases with increasing film thicknesses (Figure 1c), which is in line with experimental studies[8,9,43,44] and theoretical calculations.[45] For ideal bulk $PtSe_2$, an intensity ratio approaching 1 is expected. Here, we measured ratios close to 0.5 up to a film thickness of 15 nm, which increased to close to 0.7 for a film thickness of 23 nm. The intensity ratios vary for samples of the same thickness. The measured intensity ratios are lower than expected for bulk $PtSe_2$, suggesting that the polycrystalline TAC-grown $PtSe_2$ films consist of stacked crystallites of only very few layers each, producing a superposition of few-layer Raman signatures, with some variation between samples.

It was previously suggested that the full width at half maximum (FWHM) of the E_g peak in $PtSe_2$ is an indicator of the film quality,[33,44] similar to the FWHM of the 2D peak in graphene correlating to its charge carrier mobility.[46,47] An E_g FWHM of ≤ 7 cm^{-1} has been proposed as an indicator for high quality layered films.[44]

Histograms of the FWHM of the E_g peak were extracted from Raman area scans (Figure 1d). The FWHM varied between ≈ 4.5 and 8.5 cm^{-1} across the different samples, independent of the film thickness.

A comparison of Raman spectra of as-grown and transferred samples of batch 4 shows no major differences in peak position and peak width (Figure S1, Supporting Information). This indicates that the transfer process had no impact on the film quality.

The samples have been further analyzed with x-ray photoelectron spectroscopy (XPS) for revealing their chemical composition. The results show no significant differences in peak features (Figure S2, Supporting Information): indicating similar chemical compositions of all investigated films. Indeed, the extracted atomic ratios of Se and Pt atoms were ≈ 1.7 for samples 1, 2A, 2D, and 3 and ≈ 1.8 for samples 4A, 4B, and 4C with deviations within the measurement tolerances. Significant differences in the chemical composition of the films like oxygen content or unselenized Pt can, therefore, be ruled out.

The $PtSe_2$ films of samples 1, 2A, 2D, 3, 4A, and 4C were analyzed using annular bright field and annular dark field scanning transmission electron microscopy (ABF/ADF STEM). Cross-sectional images of the films reveal a polycrystalline structure with varying crystallite sizes and arrangements (see **Figure 2** and Figure S3: Supporting Information). The STEM images of films with similar thickness, such as samples 1 and 2A with 5 nm thickness, reveal significant differences in their nanocrystalline structure. For example, the images of sample 1 display a smooth arrangement of the $PtSe_2$ crystallites, highly oriented and parallel to the substrate (Figure 2a and Figure S3a: Supporting Information). The crystallites lateral dimensions are found to be ≈ 10 nm in size. The images of sample 2A, in contrast, reveal a film with much rougher surface and randomly oriented crystallites with lateral dimensions of ≈ 5 nm (Figure 2b and Figure S3b: Supporting Information). The images of sample 4A also show a rather smooth surface, similar to sample 1, albeit slightly smaller crystal sizes (Figure 2e and Figure S3e: Supporting Information).

The STEM images of the thicker films of samples 2D, 3, and 4C, show the atomic nanocrystalline layers only close to the SiO_2 substrate (Figure 2c,d,f and Figure S3c,d,f: Supporting Information). Crystallites in the upper parts of the films may be tilted out of the plane of the substrate and their atomic layer structure therefore becomes invisible for STEM. In the thickest of all examined films in sample 4C, several almost vertically grown crystallites are visible. Vertically aligned layers of $PtSe_2$ and other 2D dichalcogenides have been reported previously

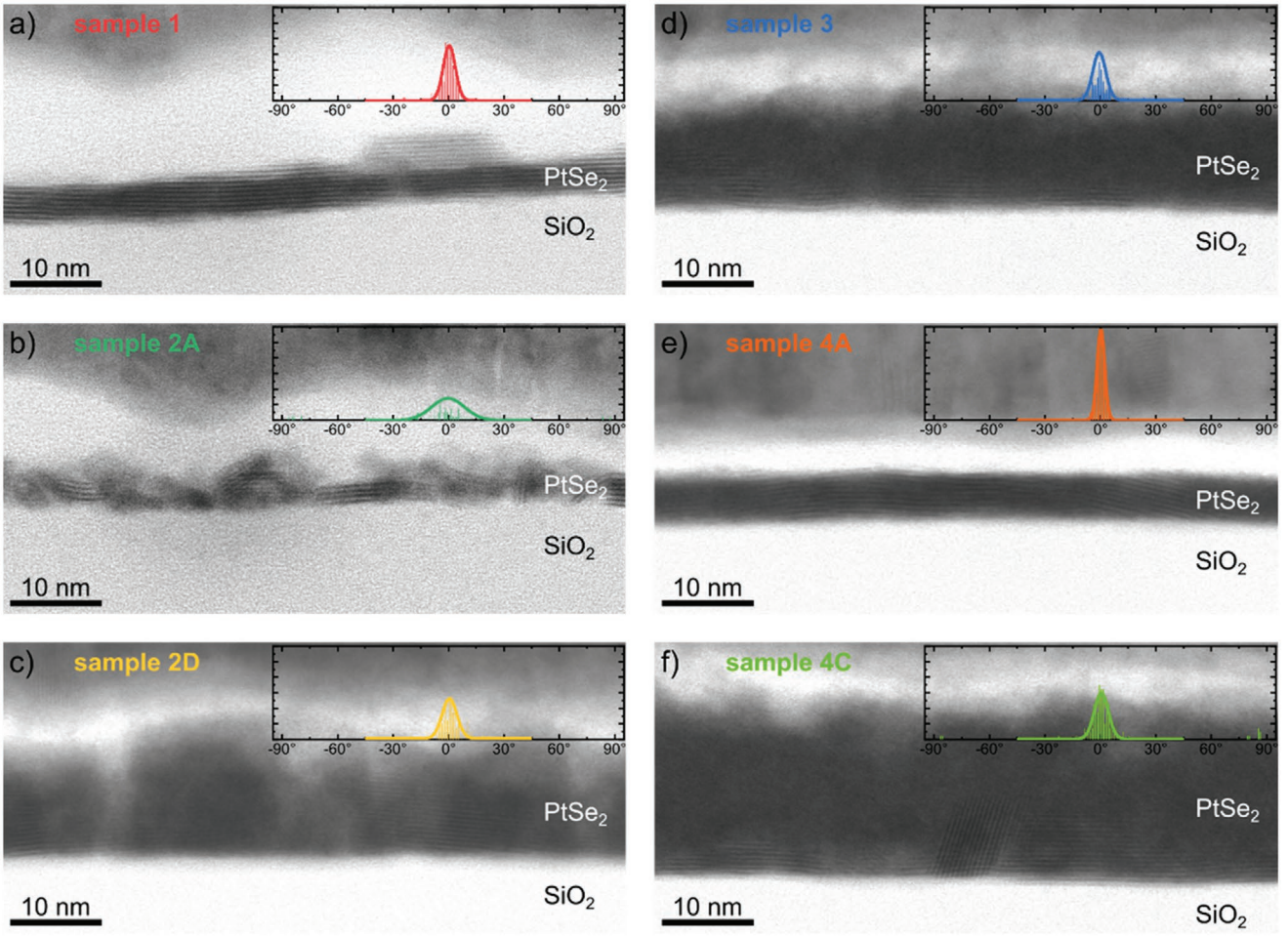

Figure 2. Annular bright field scanning transmission electron microscopy (ABF STEM) images of the $PtSe_2$ films of a) sample 1, b) sample 2A, c) sample 2D, d) sample 3, e) sample 4A, and f) sample 4C. Additional images at slightly higher magnification can be found in Figures S3 and S4 (Supporting Information). The insets show histograms with Gaussian fits of the distribution of the crystallite tilting angles (on *x*-axis) extracted from annular dark field (ADF) STEM image analysis (see also Figure S6, Supporting Information).

for thicker films.[15,48,49] The STEM investigations confirm the structural variations as indicated indirectly by the Raman spectroscopic studies discussed earlier.

When comparing the lateral dimensions of the crystallites across the different samples, sample 4C exhibits the largest crystallites with more than 10 nm lateral dimension, coinciding with the lowest Raman E_g peak FWHM measured for this sample. Samples 1, 4A, 2D, and 3 follow with similar, slightly larger E_g FWHM and similar, slightly smaller estimated crystallite sizes, and finally sample 2A shows the highest E_g FWHM while clearly possessing the smallest crystallites.

While the previous analysis was only based on the observation of individual ABF STEM images by naked eye, several images of all six samples were quantitatively analyzed using a pattern recognition feature of a software tool dedicated to automated data extraction from images (GenISys ProSEM[50]). For this purpose, the image contour lines were enhanced by suitable image filters (using ImageJ software) to facilitate the pattern recognition. Several 5 nm square sections were selected within each $PtSe_2$ image, which were then analyzed by an algorithm that yields the tilting angle of the crystallites with respect to the SiO_2 surface within each image section. The analysis of the extracted angles in 585 sections across 57 ADF STEM images resulted in the statistical distribution of tilting angles of the crystallites (see insets in Figure 2a–f). A clear difference is seen between samples 1 and 2A, which also showed the largest difference in electronic properties (see below). The tilting angles for sample 2A are much more spread than for sample 1 (standard deviation: 30.59 ° vs 6.51 °). Furthermore, some almost vertically oriented crystallites can be identified in the angle distributions for samples 2A and 4C (not included in the fit to determine the standard deviation), as previously observed in the STEM images. Automating the analysis of the STEM images has several uncertainties. Crystallites tilted out of the plane of view are not visible in STEM images and are therefore not included in the analysis. In addition, the number of analyzed image sections varies across the six examined samples, because images of well-aligned crystallites are more easily registered and subsequently analyzed by pattern recognition. Nevertheless, the statistical analysis underlines the observation of increased nanocrystalline disorder in several of the $PtSe_2$ films.

2.2. Device Fabrication and Characterization

After structural characterization, electronic devices based on transferred $PtSe_2$ films were fabricated and characterized to explore their electronic and piezoresistive properties.

Transfer length method (TLM) and six-port Hall bar structures have been defined with optical contact lithography and the $PtSe_2$ films have been patterned using CF_4/O_2-based reactive ion etching (RIE). Nickel/aluminum (Ni/Al) edge contacts have been realized through a self-aligned method.[51] The highly doped Si substrate acts as a global back gate with the 90 nm SiO_2 layer as gate dielectric. A cross-sectional schematic of such devices is shown in **Figure 3**a. SEM images of the six-port and TLM devices are shown in Figure 3c,d, respectively. Raman scans across the patterned device channels reveal the successful patterning of $PtSe_2$ device channels without noticeable damage (see Figure 3b).

TLM measurements have been performed to extract the contact resistance (R_c) and the sheet resistance ($R_\square$) of the various samples without gate bias (Figure S7, Supporting Information). The sheet resistance has additionally been measured in four-point measurements using the six-port Hall bar devices. The $R_\square$ data show a dramatic spread over several orders of magnitude between the different samples. For instance, samples with similar film thicknesses of 5 nm exhibit $R_\square$ variations of approximately four orders of magnitude, i.e., between 6 kΩ $\square^{-1}$ and more than 100 MΩ $\square^{-1}$. R_c was difficult to precisely extract for the high-ohmic samples 2A, 2B, and 4A due to large scattering of the data points. For all samples with $R_\square < 50$ kΩ $\square^{-1}$, R_c was between 0.7 and 2.1 kΩ µm.

The six-port Hall bar structures have been used to conduct back-gated field-effect measurements in a four-point set-up (**Figure 4**c). The four-point configuration allows the extraction of the charge carrier mobility (μ) without the parasitic influence of R_c,[52–56] which varied greatly in the TLM measurements. It is based on the two-point method, where the effective field-effect charge carrier mobility (μ_{2P}) can be calculated according to Equation (1),[57,58]

$$\mu_{2P} = \frac{\partial I_D}{\partial V_{BG}} \cdot \frac{1}{V_{DS}} \cdot \frac{L}{W} \cdot \frac{d_{ox}}{\varepsilon_{r,ox}\varepsilon_0} \tag{1}$$

Here, I_D is the bias-driven current through the channel, V_{BG} is the back-gate voltage, V_{DS} is the voltage applied to the channel, L is the channel length between the two contacts, $W \approx 10$ µm is the channel width, $d_{ox} = 90$ nm is the gate oxide thickness, $\varepsilon_{r,ox} = 3.9$ is the relative permittivity of the gate oxide (SiO_2), and ε_0 is the vacuum permittivity. In the four-point configuration, the two inner contacts are used to measure the differential voltage between the two neighboring inner contacts (V_{diff}), which replaces V_{DS} in Equation (1). Since V_{diff} may change with V_{BG}, it must be placed in the derivative. The effective field-effect charge carrier mobility (μ_F) in the four-point set-up can then be extracted according to Equation (2),

$$\mu_F = \frac{\partial(I_D/V_{diff})}{\partial V_{BG}} \cdot \frac{L_{inner}}{W} \cdot \frac{d_{ox}}{\varepsilon_{r,ox}\varepsilon_0} \tag{2}$$

This extraction method leads to a macroscopic value of the effective mobility of the polycrystalline material, whereas the

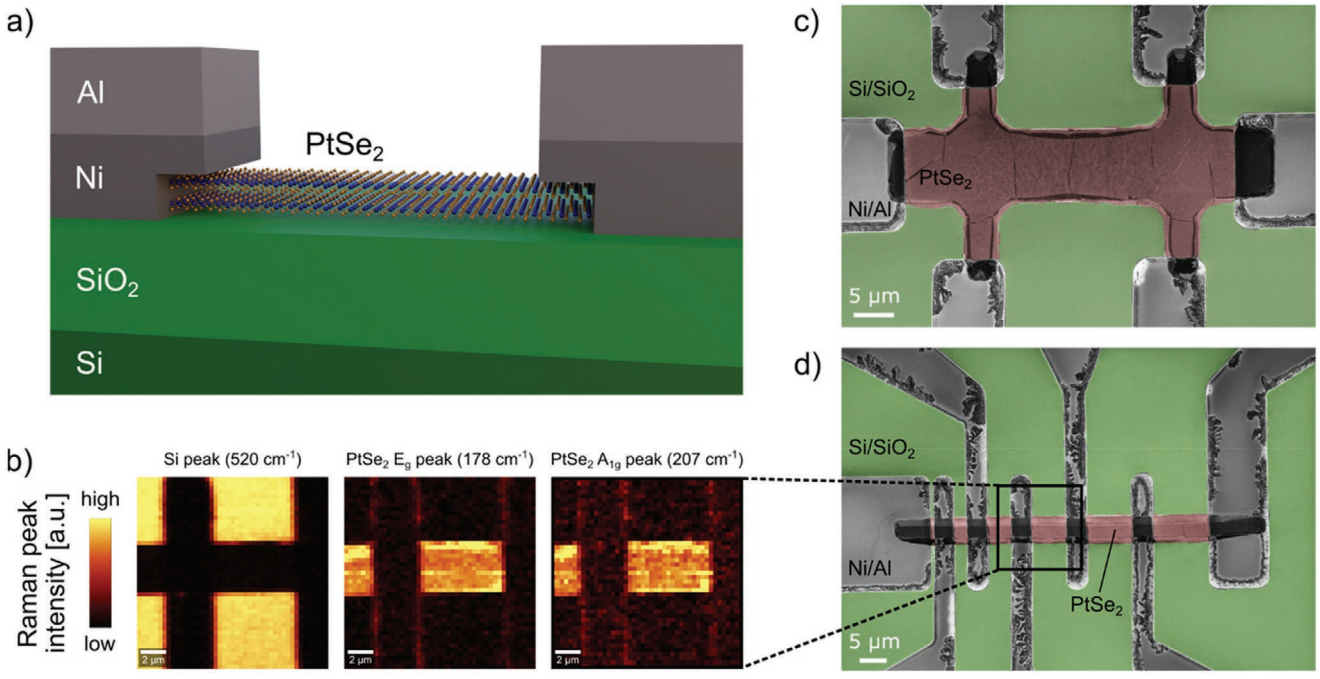

Figure 3. a) Schematic cross section of the $PtSe_2$ devices. b) Raman maps of the intensities of the Si peak (520 cm^{-1}), and the E_g and A_{1g} peaks of $PtSe_2$ after etching the $PtSe_2$ for channel patterning of a TLM device. The bright, yellow pixels represent high intensity of the respective peak, while the dark pixels represent low intensity. c) False-color SEM images of a six-port device and d) a TLM device. The $PtSe_2$ channel is shown in red and the SiO_2 substrate is shown in green.

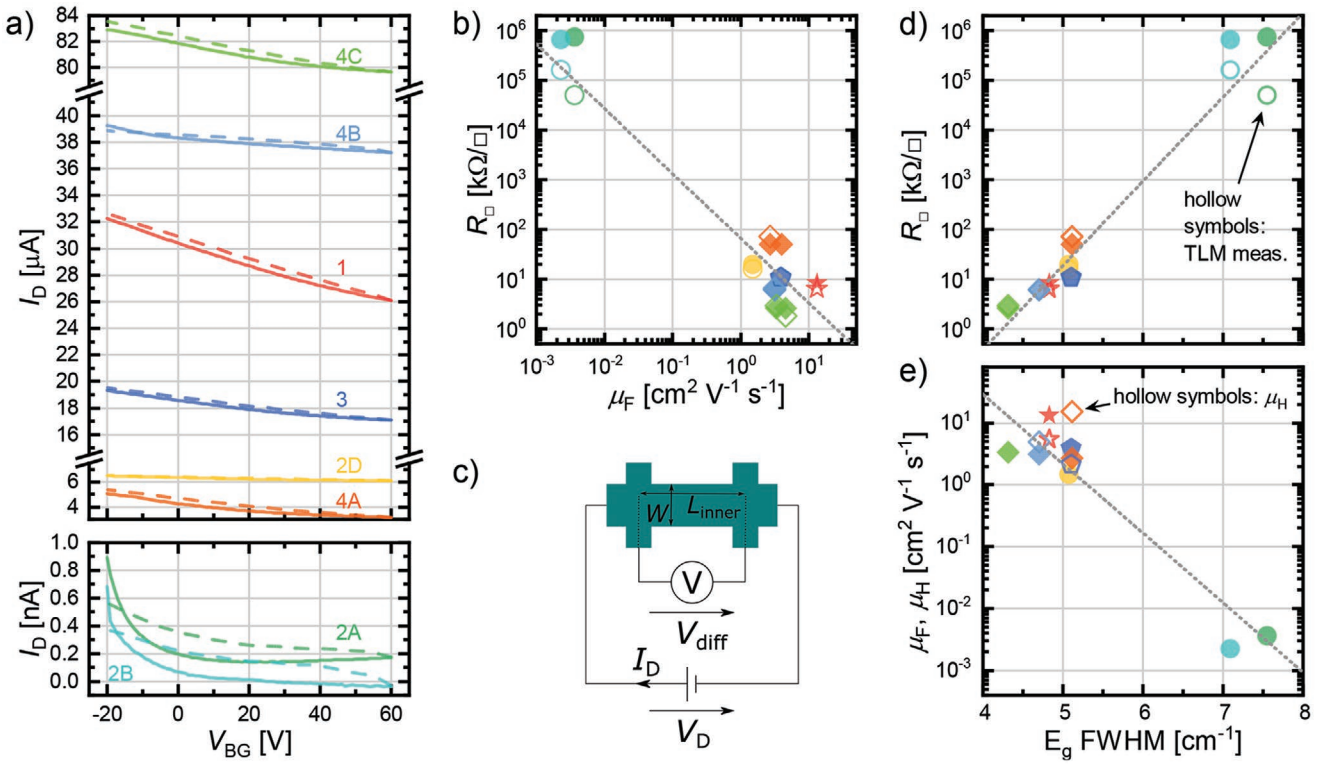

Figure 4. a) Field-effect measurements of the various $PtSe_2$ devices. The back-gate voltage V_{BG} was swept from −20 to 60 V (solid line) and back (dashed line). Sample numbers are indicated. b) Correlation between the field-effect mobility μ_F and the sheet resistance $R_\square$. $PtSe_2$ samples with a high $R_\square$ exhibit a low μ_F and vice versa. The filled and hollow symbols correspond to four-point and TLM measurements, respectively. c) Schematic of the four-point set-up used for field-effect mobility and sheet resistance extraction. d) Exponential dependence of the sheet resistance $R_\square$ on the Raman E_g peak FWHM. The filled and hollow symbols correspond to four-point and TLM measurements, respectively. e) Dependence of the field-effect mobility μ_F (solid symbols) and the Hall mobility μ_H (hollow symbols) on the Raman E_g peak FWHM. In all panels, the dotted lines are just a guide to the eye. Sample numbers are color-coded in panel (a) and indicated in Table 1.

intrinsic mobility of individual single-crystal $PtSe_2$ will certainly be higher, as reported from experimental studies on exfoliated $PtSe_2$.[13,21] All devices showed p-type behavior as their resistance decreased with negative gate bias (Figure 4a). Large variations in μ_F were measured, ranging from below 0.005 cm^2 V^{-1} s^{-1} (samples 2A and 2B) up to more than 13 cm^2 V^{-1} s^{-1} (sample 1) on samples of similar $PtSe_2$ film thickness. Note that for samples 2A and 2B, the gate and the drain current were of similar magnitude (< 0.5 nA), as shown in Figure S8 (Supporting Information). Therefore, the corresponding mobility measurements must be treated with caution. In general, the lowest mobilities were measured in films of poor crystalline quality, according to the TEM and Raman analysis. The $R_\square$ values are plotted as a function of the extracted μ_F in Figure 4b, which illustrates an obvious correlation between the two macroscopic values.

Note that for batch 4, $R_\square$, R_c, and μ_F have been extracted from devices of both as-grown and transferred films with no significant differences observed. As already seen from the Raman spectra of batch 4 samples, the transfer method does therefore not significantly modify the $PtSe_2$ film quality.

The extracted electronic properties like sheet resistance and carrier mobility correlate well with the E_g peak FWHM as retrieved from Raman analysis, with an exponential and inverse exponential dependence, respectively (Figure 4d,e). Film thickness alone is thus clearly not a suitable measure to predict the electronic properties of TAC-grown $PtSe_2$. Raman spectroscopy can provide additional insights into expected electronic properties of $PtSe_2$. However, judging from our experiments, high quality TAC-grown $PtSe_2$ films should exhibit an E_g FWHM of < 5 cm^{-1}.

AC-modulated Hall effect measurements were performed on four samples with sufficiently high μ_F (sample numbers 1, 3, 4A and 4B), since the generally low effective mobilities did not result in Hall signals in a standard DC Hall set-up. Hall voltages on the order of a few 100 µV have been extracted from the AC Hall signal (see Figure S9b in the Supporting Information), which corresponds to effective Hall mobilities between 2.1 and 15.3 cm^2 V^{-1} s^{-1} (see Table 1 for details). The extracted sheet charge carrier densities ($n_\square$) were between 7.3 × 10^{12} and 2.9 × 10^{14} cm^{-2} in line with previous Hall data in $PtSe_2$ devices.[22] The polarity of the measured Hall voltages confirmed that the $PtSe_2$ samples were p-type. However, we cannot rule out the presence of both holes and electrons in the samples, which is why the reported μ_H and $n_\square$ should be treated with caution.

The temperature-dependence of the resistance can give insights into the details of the charge transport inside the material. $R_\square$ of several $PtSe_2$ devices on SiO_2 substrates was therefore measured at predefined temperatures up to 100 °C in ambient conditions in the four-point set-up. All devices displayed a decrease of $R_\square$ with increasing temperature, typical

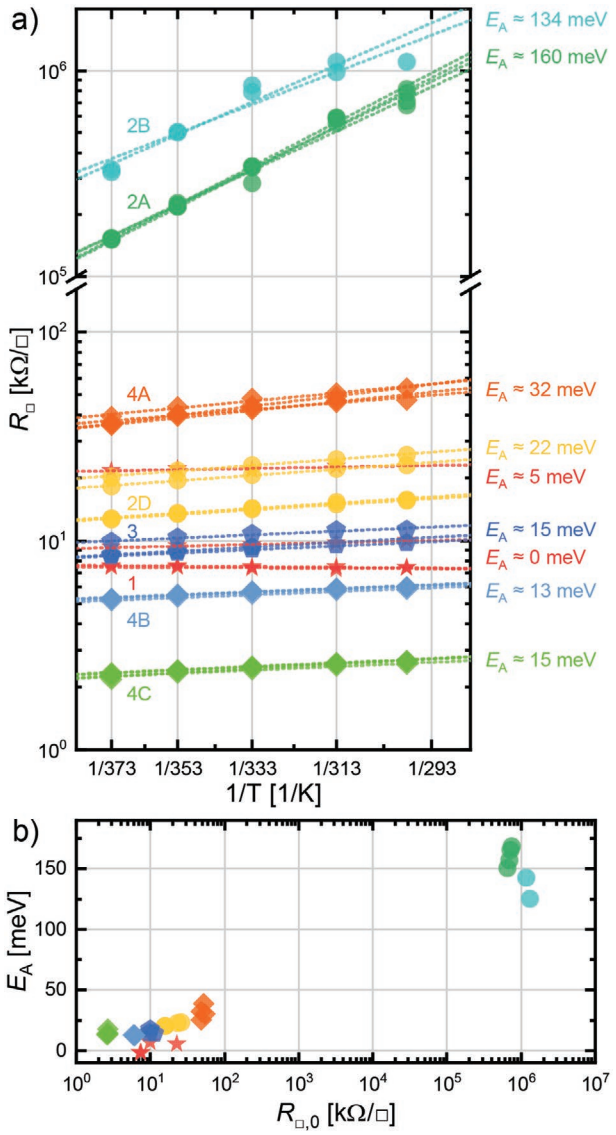

Figure 5. Temperature dependence of the sheet resistance $R_\square$. a) Arrhenius plot of the temperature dependence of $R_\square$ of 29 measured devices. The measurements were done without applied back-gate voltage (floating gate). An exponential dependence of $R_\square$ on the inverse temperature is seen, which is a sign of an energy barrier that the charge carriers need to overcome. We suggest that this barrier may be caused by the grain boundaries in the polycrystalline film. Fits are shown as dotted lines and average extracted activation energies E_A are shown for each sample. b) Dependence of the extracted activation energy E_A on the initial sheet resistance at $T = 25$ °C. Sample numbers are indicated in panel (a) and in Table 1.

for temperature-dependent carrier transport in semiconducting crystals[24] and similar to previously observed behavior in $PtSe_2$ at a lower temperatures.[26] This is an indication that the nanocrystalline $PtSe_2$ films are of semiconducting nature, at least partially. Note that the resistance values went back to their original level after cool-down. The data points were fitted to a linear curve according to Equation (3),[59]

$$R_\square = R_{\square,0}\left(1+\alpha_{lin}\left(T-T_0\right)\right) \quad (3)$$

where $R_{\square,0}$ is the sheet resistance at the reference temperature $T_0 = 25$ °C. The data is shown in Figure S10a (Supporting Information). The temperature coefficient of resistance, α_{lin}, was determined to range from zero (i.e., no variation with temperature) to ≈ –0.012 K^{-1} for measurements without applying a back-gate voltage. By absolute value, devices with the lowest $R_\square$ had the lowest α_{lin}, and the absolute value of α_{lin} increased toward higher $R_\square$. This trend is observed over a $R_\square$ range of almost six orders of magnitude (see Figure S10b in the Supporting Information). An Arrhenius plot in **Figure 5**a was fitted with Equation (4),

$$\ln\left(\frac{R_\square}{1\ \mathrm{k\Omega/\square}}\right) = m\frac{1}{T}+\gamma_0 \quad (4)$$

Here, m is the slope and γ_0 is the y-axis intercept of the fit. From the slope, an activation energy (E_A) can be calculated according to $m = E_A/k_B$ where k_B is the Boltzmann constant. In this way, $R_\square$ follows as Equation (5),

$$R_\square = R_{\square,\infty}\ e^{\frac{E_A}{k_B T}} \quad (5)$$

with the fitting parameter $R_{\square,\infty} = 1\ \mathrm{k\Omega}\ \square^{-1} \times e^{\gamma_0}$.We interpret E_A as a measurement of the inter-grain barrier height. A clear correlation with the extracted $R_\square$ is evident (Figure 5b), very similar to the relationship of α_{lin} and $R_\square$. The extracted E_A ranges from zero to 32 meV for all low-resistance samples ($R_\square < 100\ \mathrm{k\Omega}\ \square^{-1}$) and increases up to 160 meV for the extremely high-resistance samples with almost gigaohm-range $R_\square$. These higher values are in agreement with previous work on transferred TAC-grown $PtSe_2$, where an activation energy of ≈ 200 meV was extracted at zero gate voltage[22] and with work on pristine TAC grown $PtSe_2$, where an activation energy of 134 meV was reported.[24] In the latter, a decrease of E_A is attributed to an Ar plasma treatment and a resulting reduction of the Se content in their samples. This is in contrast to our samples, where the ratio of Pt and Se was determined to be approximately the same in XPS measurements for samples of very different E_A. Furthermore, we observe a decrease of E_A in the ON state, i.e., at negative back-gate voltages (Figure S11, Supporting Information), for both as-grown and for transferred films. Previously, this effect has been observed only after transfer of $PtSe_2$, but not for as-grown films.[22] The effect is small for samples 4B and 4C, but more pronounced for sample 4A, where E_A changes from 25 meV in the ON-state to 45 meV in the OFF-state. However, our non-transferred samples generally exhibit a lower E_A than those in.[22]

The piezoresistive gauge factor (GF) of $PtSe_2$ is an important parameter for membrane-based sensor applications. The GF was determined using unpatterned $PtSe_2$ films transferred to flexible substrates glued to a steel beam with an attached mass. The set-up is described in detail in the methods section and in [2]. The direction of current flow through the $PtSe_2$ films was parallel to the direction of mechanical strain due to the bending of the steel beam. A constant DC voltage was applied while the total resistance of the films was monitored during loading and unloading of the beam with a mass of 2 kg. Resistance changes upon mechanical strain were evident for all $PtSe_2$ films,

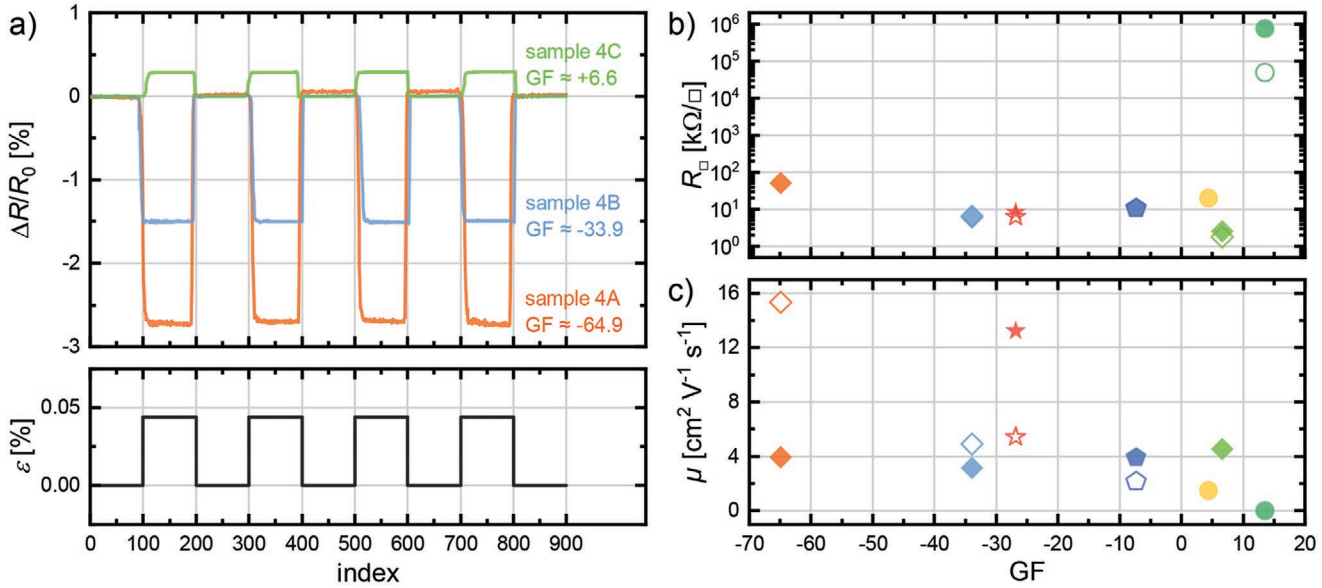

Figure 6. a) Measurements of the change of device resistance $\Delta R/R_0$ under applied strain over time, shown for three samples of material batch 4. The bottom panel shows the applied tensile strain ε. One curve was recorded within ≈2 min. b) Correlation of the piezoresistive gauge factor (GF) and the sheet resistance $R_\square$. The filled and hollow symbols correspond to four-point and TLM measurements, respectively. c) Correlation of GF and the extracted effective charge carrier mobility μ. Here, the filled and hollow symbols correspond to μ_F and μ_H, respectively. Sample numbers are indicated in Table 1.

although their magnitude and even their sign varied. The GF can generally be calculated with Equation (6),[60]

$$\mathrm{GF} = \frac{\Delta R}{R_0 \varepsilon} = 1 + 2\nu + \frac{\Delta \rho}{\rho_0 \varepsilon} \tag{6}$$

where ΔR is the difference between the initial resistance R_0 without strain and the resistance under the strain ε at the position of the sample. Furthermore, ν is Poisson's ratio, $\Delta\rho$ is the change in resistivity from the initial resistivity ρ_0 under the strain ε. Therefore, $1 + 2\nu$ is the geometric contribution and $\Delta\rho/\rho_0\varepsilon$ is the piezoresistive contribution to GF. Tensile (positive) or compressive (negative) strain can be applied by mounting the sample on the top or bottom of the beam, respectively. For an applied mass of 2 kg, the strain is $\varepsilon \approx \pm 4.4 \times 10^{-4} = \pm 0.044\%$, as calculated in [2]. In the following, the average GF from measurements with tensile and compressive strain are reported. As with the resistance and mobility values, the spread in GF is large, ranging from –64.9 to +13.5 across seven measured samples. While single-digit positive GF are typical for metals such as aluminum, copper, gold, iron, platinum, or silver,[61] and originate mainly from the geometrical contribution of the equation, the piezoresistive contribution can dominate the equation in semiconductors and lead to a negative GF. In the latter case, changes in the band structure cause changes in the mobility and the charge carrier density, for example in silicon or germanium, where the GF can vary from less than –150 to more than +150, depending on the crystalline orientation and doping.[61] Due to the high negative GFs observed in some of the present polycrystalline $PtSe_2$ films, they are likely to include semiconducting crystallites, in line with the evidence provided through the temperature dependent transport measurements. In addition, the arrangement of the crystallites in the film is expected to have an influence on the GF, as the applied strain can change the grain overlap area through small shifts of the crystallite positions, similar to graphene flakes on graphene-ink coated substrates.[62]

In **Figure 6**b, the measured $R_\square$ is plotted versus the GF. No clear correlation can be observed, in particular for samples with low sheet resistance. The situation is different when plotting the carrier mobility versus the GF (Figure 6c). Here, higher negative GFs are generally observed for higher mobility samples, in particular when considering Hall mobility data. The field effect mobility data of samples 4A, 4B, and 4C does not fit this trend, as they show different, negative and positive GFs at similar μ_F, although their growth process only differs in the thickness of the initial Pt layer. For samples 4A, 4B, and 4C, the GF increases with film thickness, a trend that is not generally confirmed by our data. In contrast, distinctly different electronic and piezoresistive behavior have been observed in samples of similar thickness as well as growth and processing conditions. Samples 1 and 2A in particular show variations by many orders of magnitude.[63]

The STEM images do not present a full explanation to the variation of the GF. It appears that the GF is influenced by both the total film thickness and the nanocrystalline structure. We observe high negative values of the GF for well-aligned, thin films of $PtSe_2$ (< 10 nm, samples 1 and 4A), and low positive values of the GF for generally thicker and less well aligned films (samples 4C and 2D). A thin but very disordered film (sample 2A), however, results in a positive GF as well.

The correlation between GFs and the electronic and material properties in TAC is a complex issue and cannot be explained by assuming ideal 2D layered $PtSe_2$. In addition, the GF is related to the change of the product of charge carrier density and mobility with strain in conventional, 3D semiconductors,[61]

data that could not be extracted from the experiments conducted in this work.

2.3. Modelling

The correlation between the electronic properties and the polycrystalline structure of a material can be explained through the size and number of the grain boundaries, acting as tunnel barriers for the charge carriers. Experience from research on other 2D materials such as graphene[35,36] or MoS_2[37,38] suggests that the resistivity and the effective mobility are influenced by the sizes of individual crystallites and their respective orientation. However, these materials are commonly grown by chemical vapor deposition yielding grains on micrometer scale or larger. Therefore, grain boundaries are likely to make up a significant part of the film and therefore can be expected to play a major role in determining the electronic properties, competing with the intrinsic electrical properties of the material.

Assuming similar chemical composition of the films and negligible differences during device fabrication, two properties influence $R_{\square}$. One factor is the average grain size, correlating with the number of grain boundaries in the film. A second factor is the barrier height presented by the grain boundaries. In our $PtSe_2$ films, the effects can be captured in a resistivity model for polycrystalline films,[41,42] which qualitatively captures the experimental observations of an increase in resistivity for a film with both decreasing crystallite size and increasing grain boundary density. The model is described in detail in Figure S13 in the Supporting Information.

The change of resistivity upon heating can also be understood with the above-mentioned model. From Figure S13b (Supporting Information), it is evident that even a minor change in the reflectivity coefficient (r) of the grain boundary barrier, possibly enforced through an increase in kinetic energy of the charge carriers, i.e., a higher temperature of the polycrystalline film, can greatly influence the polycrystalline resistivity. This underlines the significance of controlling the nanocrystalline structure, especially the amount and size of grain boundaries, in TAC-based growth processes.

3. Conclusion

We have demonstrated that the electronic properties of TAC-grown $PtSe_2$ films greatly depend on the nanocrystalline structure of the materials. Correlations between structure and electronic properties are discussed based on detailed Raman and TEM studies and electrical measurements. Cross-sectional TEM images reveal that TAC-grown $PtSe_2$ films are composed of crystallites of varying size, thickness, and orientation. Thus, the thickness of a TAC-grown $PtSe_2$ film does not directly translate to the number of atomic layers in each crystallite, i.e., it does not imply the electronic properties on its own. The characteristic Raman peaks (especially FWHM of E_g peak) correlate well with the measured electronic sheet resistance across many orders of magnitude and are reasonably well in line with the extracted effective charge carrier mobility. Our $PtSe_2$ samples exhibit both positive and negative piezoresistive gauge factors and show signs of both metallic and semiconducting behavior. The sign and magnitude of the GF are affected by both the material structure and the total film thickness. Our results suggest that the properties of $PtSe_2$ films can be tailored by controlling their nanocrystalline structure, which requires great control of the TAC process. For example, applications in nanoelectromechanical systems such as strain, pressure or acceleration sensors or microphones would benefit from high negative piezoresistive gauge factors, such as demonstrated here in very thin $PtSe_2$ films. We conclude that TAC growth processes, which have been previously shown to be scalable and manufacturable, can be tuned to design application-specific $PtSe_2$ and other 2D material films.

4. Experimental Section

Material Synthesis: Platinum (Pt) layers of varying thickness were deposited (sputtered or evaporated) onto the centimeter-sized SiO_2 or quartz growth substrates. TAC was used to convert the initial metal layers forming $PtSe_2$ as published earlier.[1,8]

The film thicknesses were either determined from the initially deposited layer of Pt prior to selenization (by multiplication with the expansion factor[23]), by means of AFM, or from the TEM analysis.

Raman Characterization: The Raman measurements were performed using a WITec alpha 300R system with a 532 nm laser and a 1800 g mm^{-1} grating. The laser power was set to 300 µW. The lateral resolution of the system was limited to 300 nm. The FWHM was extracted from Lorentzian fits of the Raman peaks. For a statistical analysis, area scans were performed and the position and FWHM were extracted from Gaussian histogram fits. Calibration was done using the Si peak at 520 cm^{-1}.

XPS Characterization: For XPS measurements, a PHI VersaProbe III instrument equipped with a micro-focused monochromated Al Kα source (1486.6 eV) and dual beam charge neutralization was used. High-resolution scans of the individual core-orbitals of interest including platinum (Pt), selenium (Se), carbon (C), and oxygen (O) were obtained. The binding energy was referenced to the Pt 4f 7/2 level and set to 73.65 eV. The common practice of using the C 1s level for reference was avoided due to the strong Kapton signal overlapping the adventitious C peak. Choosing the Pt 4f 7/2 level energy of 73.65 eV as fixed value is in agreement with comparable $PtSe_2$ films on other substrates were the adventitious C reference could be used.

TEM Sample Preparation and Characterization: TEM lamellae were prepared using a focused ion beam (FIB) technique employing two different FEI Dual Beam Helios NanoLab systems causing different quality of final lamellae. The lamellae of samples 1 and 2A were thinner, which is why the final images look clearer. The annular bright field and annular dark field scanning transmission electron microscopy (ABF and ADF STEM) was carried out on an FEI Titan 80–300 probe Cs-corrected TEM operated at 200 kV.[64]

Device Fabrication and Characterization: The $PtSe_2$ films of material batches 1, 2, and 3 were transferred from their growth substrates onto Si/SiO_2 (90 nm) substrates using a potassium hydroxide (KOH) based wet transfer technique. A supporting layer of poly(methyl methacrylate) (PMMA) was applied to the $PtSe_2$ films and the film was scratched to provide access to the underlying oxide layer to a few drops of a KOH solution. After delamination, the $PtSe_2$/PMMA films remained floating on the surface of DI water from where they were transferred onto the final substrates by a fishing technique. The samples were dried in air and the PMMA support layer was then removed in acetone and IPA. For material batch 4, device fabrication was done on the growth substrates, which already were the same Si/SiO_2 (90 nm) substrates. Transfer length method (TLM) and six-port Hall bar structures were then fabricated using contact lithography and a CF_4/O_2-based reactive ion etching (RIE)

process. In the first lithography step, the self-aligned edge contacts[51] were fabricated by first etching the $PtSe_2$ under the contact pads and then sputtering Ni and Al, followed by a lift-off process. Afterward, the $PtSe_2$ channels were defined in a second lithography and etching step. The channel width and length of the Hall bar structures (W and L_{inner}) were measured after device fabrication for each sample individually by optical microscopy.

Hall Measurements: A bias current I_C was applied to the outer contacts of the six-port Hall bar devices and the Hall voltage V_H between two opposite inner contacts was measured over time while the magnetic field B was switched on and off (Figure S9a, Supporting Information). From the Hall effect measurements, the current and voltage related sensitivities S_I and S_V can be extracted according to Equations (7) and (8),

$$S_I = \frac{1}{I_C}\left|\frac{\partial V_H}{\partial B}\right| \tag{7}$$

$$S_V = \frac{1}{V_C}\left|\frac{\partial V_H}{\partial B}\right| \tag{8}$$

where V_C is the voltage between the two outer contacts resulting from the current bias. The sheet charge carrier density $n_\square$ and the effective Hall mobility μ_H can then be extracted according to Equations (9) and (10),[65,66]

$$n_\square = \frac{1}{S_I e} \tag{9}$$

$$\mu_H = S_V \frac{L}{W} \tag{10}$$

where e is the elementary charge, $L \approx 40$ µm is the total channel length, and $W \approx 10$ µm is the channel width. A lock-in amplifier (Stanford Research Systems Model SR830 DSP Lock-In Amplifier) was used to provide a sine wave signal with an amplitude of 5 V and a frequency of ≈ 45 Hz as bias on the outer contacts. For the integration of the measured Hall signal, a time constant of 300 ms was chosen. The magnetic field was switched between −57.6 and +57.6 mT to maximize the output signal.

Strain Gauge Fabrication and Characterization: Large metal contacts (Ni) were sputtered onto pieces of flexible polyimide foil (Kapton) using a shadow mask. The $PtSe_2$ films were then transferred from their growth substrates onto the polyimide foil with the same technique as described above, resulting in unpatterned strain gauges of millimeter size with bottom contacts. The PMMA from the transfer was removed from the $PtSe_2$ but a new layer of PMMA was spin-coated and baked at 115 °C for 10 min after the transfer to protect the devices from mechanical stress during the following steps. Electrical measurements showed that the additional PMMA layer did not significantly affect the resistance of the strain gauges. All samples were then glued to the steel beam (300 mm × 30 mm × 3 mm) with a distance of 200 mm to the loading point. The applied mechanical strain was calculated and simulated depending on the attached load in the same way as done previously.[2] The measurement set-up is shown in Figure S12 (Supporting Information), including a video recording of a measurement.

Supporting Information

Supporting Information is available from the Wiley Online Library or from the author.

Acknowledgements

This work has received funding from the German Ministry of Education and Research (BMBF) under grant agreement 16ES1121 (ForMikro-NobleNEMS) and from the European Union's Horizon 2020 research and innovation programme under grant agreements 829035 (QUEFORMAL), 825272 (ULISSES), 881603 (Graphene Flagship Core 3), and 881603 (GREAT).

Open access funding enabled and organized by Projekt DEAL.

Conflict of Interest

The authors declare no conflict of interest.

Data Availability Statement

Research data are not shared.

Keywords

2D materials, gauge factor, nanocrystalline materials, platinum diselenide, Raman spectroscopy, thermally assisted conversion, transition-metal dichalcogenides

Received: March 26, 2021
Revised: May 1, 2021
Published online:

[1] C. Yim, K. Lee, N. McEvoy, M. O'Brien, S. Riazimehr, N. C. Berner, C. P. Cullen, J. Kotakoski, J. C. Meyer, M. C. Lemme, G. S. Duesberg, *ACS Nano* **2016**, *10*, 9550.
[2] S. Wagner, C. Yim, N. McEvoy, S. Kataria, V. Yokaribas, A. Kuc, S. Pindl, C.-P. Fritzen, T. Heine, G. S. Duesberg, M. C. Lemme, *Nano Lett.* **2018**, *18*, 3738.
[3] C. Yim, N. McEvoy, S. Riazimehr, D. S. Schneider, F. Gity, S. Monaghan, P. K. Hurley, M. C. Lemme, G. S. Duesberg, *Nano Lett.* **2018**, *18*, 1794.
[4] G. Wang, Z. Wang, N. McEvoy, P. Fan, W. J. Blau, *Adv. Mater.* **2021**, *33*, 2004070.
[5] Y. Wang, Z. Yu, Y. Tong, B. Sun, Z. Zhang, J.-B. Xu, X. Sun, H. K. Tsang, *Appl. Phys. Lett.* **2020**, *116*, 211101.
[6] M. Sajjad, E. Montes, N. Singh, U. Schwingenschlögl, *Adv. Mater. Interfaces* **2017**, *4*, 1600911.
[7] Y. Wang, L. Li, W. Yao, S. Song, J. T. Sun, J. Pan, X. Ren, C. Li, E. Okunishi, Y.-Q. Wang, E. Wang, Y. Shao, Y. Y. Zhang, H. Yang, E. F. Schwier, H. Iwasawa, K. Shimada, M. Taniguchi, Z. Cheng, S. Zhou, S. Du, S. J. Pennycook, S. T. Pantelides, H.-J. Gao, *Nano Lett.* **2015**, *15*, 4013.
[8] M. O'Brien, N. McEvoy, C. Motta, J.-Y. Zheng, N. C. Berner, J. Kotakoski, K. Elibol, T. J. Pennycook, J. C. Meyer, C. Yim, M. Abid, T. Hallam, J. F. Donegan, S. Sanvito, G. S. Duesberg, *2D Mater.* **2016**, *3*, 021004.
[9] J. Shi, Y. Huan, M. Hong, R. Xu, P. Yang, Z. Zhang, X. Zou, Y. Zhang, *ACS Nano* **2019**, *13*, 8442.
[10] K. Zhang, M. Yan, H. Zhang, H. Huang, M. Arita, Z. Sun, W. Duan, Y. Wu, S. Zhou, *Phys. Rev. B* **2017**, *96*, 125102.
[11] L. Li, K. Xiong, R. J. Marstell, A. Madjar, N. C. Strandwitz, J. C. M. Hwang, N. McEvoy, J. B. McManus, G. S. Duesberg, A. Goritz, M. Wietstruck, M. Kaynak, *IEEE Trans. Electron Devices* **2018**, *65*, 4102.
[12] T.-Y. Su, H. Medina, Y.-Z. Chen, S.-W. Wang, S.-S. Lee, Y.-C. Shih, C.-W. Chen, H.-C. Kuo, F.-C. Chuang, Y.-L. Chueh, *Small* **2018**, *14*, 1800032.
[13] Y. Yang, S. K. Jang, H. Choi, J. Xu, S. Lee, *Nanoscale* **2019**, *11*, 21068.

[14] W. Zhang, Z. Huang, W. Zhang, Y. Li, *Nano Res.* **2014**, *7*, 1731.
[15] S. S. Han, J. H. Kim, C. Noh, J. H. Kim, E. Ji, J. Kwon, S. M. Yu, T.-J. Ko, E. Okogbue, K. H. Oh, H.-S. Chung, Y. Jung, G.-H. Lee, Y. Jung, *ACS Appl. Mater. Interfaces* **2019**, *11*, 13598.
[16] H. Xu, H. Zhang, Y. Liu, S. Zhang, Y. Sun, Z. Guo, Y. Sheng, X. Wang, C. Luo, X. Wu, J. Wang, W. Hu, Z. Xu, Q. Sun, P. Zhou, J. Shi, Z. Sun, D. W. Zhang, W. Bao, *Adv. Funct. Mater.* **2019**, *29*, 1805614.
[17] X. Yu, P. Yu, Z. Liu, Q. J. Wang, in *2016 Conf. on Lasers and Electro-Optics CLEO*, OSA Publishing, Massachusetts **2016**, pp. 1–2.
[18] K. Zhou, J. Shen, X. Li, X. Hong, W. Feng, X. Tang, X. Jiang, D. Wei, Y. Chen, X. Liu, Y. Xie, D. Wei, T. Sun, *Phys. E* **2020**, *123*, 114147.
[19] A. Kandemir, B. Akbali, Z. Kahraman, S. V. Badalov, M. Ozcan, F. Iyikanat, H. Sahin, *Semicond. Sci. Technol.* **2018**, *33*, 085002.
[20] M. C. Lemme, S. Wagner, K. Lee, X. Fan, G. J. Verbiest, S. Wittmann, S. Lukas, R. J. Dolleman, F. Niklaus, H. S. J. van der Zant, G. S. Duesberg, P. G. Steeneken, *Research* 8748602, **2020**, *2020*.
[21] Y. Zhao, J. Qiao, Z. Yu, P. Yu, K. Xu, S. P. Lau, W. Zhou, Z. Liu, X. Wang, W. Ji, Y. Chai, *Adv. Mater.* **2017**, *29*, 1604230.
[22] L. Ansari, S. Monaghan, N. McEvoy, C. Ó. Coileáin, C. P. Cullen, J. Lin, R. Siris, T. Stimpel-Lindner, K. F. Burke, G. Mirabelli, R. Duffy, E. Caruso, R. E. Nagle, G. S. Duesberg, P. K. Hurley, F. Gity, *npj 2D Mater. Appl.* **2019**, *3*, 33.
[23] C. Yim, V. Passi, M. C. Lemme, G. S. Duesberg, C. Ó. Coileáin, E. Pallecchi, D. Fadil, N. McEvoy, *npj 2D Mater. Appl.* **2018**, *2*, 5.
[24] M. S. Shawkat, J. Gil, S. S. Han, T.-J. Ko, M. Wang, D. Dev, J. Kwon, G.-H. Lee, K. H. Oh, H.-S. Chung, T. Roy, Y. Jung, Y. Jung, *ACS Appl. Mater. Interfaces* **2020**, *12*, 14341.
[25] F. Urban, F. Gity, P. K. Hurley, N. McEvoy, A. Di Bartolomeo, *Appl. Phys. Lett.* **2020**, *117*, 193102.
[26] K. Zhang, M. Wang, X. Zhou, Y. Wang, S. Shen, K. Deng, H. Peng, J. Li, X. Lai, L. Zhang, Y. Wu, W. Duan, P. Yu, S. Zhou, *Nano Res.* 1663, **2020**, *14*.
[27] C. S. Boland, C. Ó. Coileáin, S. Wagner, J. B. McManus, C. P. Cullen, M. C. Lemme, G. S. Duesberg, N. McEvoy, *2D Mater.* **2019**, *6*, 045029.
[28] A. Ciarrocchi, A. Avsar, D. Ovchinnikov, A. Kis, *Nat. Commun.* **2018**, *9*, 919.
[29] X. Yu, P. Yu, D. Wu, B. Singh, Q. Zeng, H. Lin, W. Zhou, J. Lin, K. Suenaga, Z. Liu, Q. J. Wang, *Nat. Commun.* **2018**, *9*, 1545.
[30] M. Sojková, E. Dobročka, P. Hutár, V. Tašková, L. Pribusová Slušná, R. Stoklas, I. Píš, F. Bondino, F. Munnik, M. Hulman, *Appl. Surf. Sci.* **2021**, *538*, 147936.
[31] A. Di Bartolomeo, F. Urban, E. Faella, A. Grillo, A. Pelella, F. Giubileo, N. McEvoy, F. Gity, P. K. Hurley, *Mater. Proc.* **2020**, *4*, 28.
[32] K. Xiong, M. Hilse, L. Li, A. Göritz, M. Lisker, M. Wietstruck, M. Kaynak, R. Engel-Herbert, A. Madjar, J. C. M. Hwang, *IEEE Trans. Electron Devices* **2020**, *67*, 796.
[33] W. Jiang, X. Wang, Y. Chen, G. Wu, K. Ba, N. Xuan, Y. Sun, P. Gong, J. Bao, H. Shen, T. Lin, X. Meng, J. Wang, Z. Sun, *InfoMat* **2019**, *1*, 260.
[34] M. Hilse, K. Wang, R. Engel-Herbert, *2D Mater.* 045013, **2020**, *7*.
[35] A. Isacsson, A. W. Cummings, L. Colombo, L. Colombo, J. M. Kinaret, S. Roche, *2D Mater.* **2016**, *4*, 012002.
[36] T. Ma, Z. Liu, J. Wen, Y. Gao, X. Ren, H. Chen, C. Jin, X.-L. Ma, N. Xu, H.-M. Cheng, W. Ren, *Nat. Commun.* **2017**, *8*, 14486.
[37] T. H. Ly, D. J. Perello, J. Zhao, Q. Deng, H. Kim, G. H. Han, S. H. Chae, H. Y. Jeong, Y. H. Lee, *Nat. Commun.* **2016**, *7*, 10426.
[38] R. G. Mendes, J. Pang, A. Bachmatiuk, H. Q. Ta, L. Zhao, T. Gemming, L. Fu, Z. Liu, M. H. Rümmeli, *ACS Nano* **2019**, *13*, 978.
[39] R. Zhuo, L. Zeng, H. Yuan, D. Wu, Y. Wang, Z. Shi, T. Xu, Y. Tian, X. Li, Y. H. Tsang, *Nano Res.* **2019**, *12*, 183.
[40] Y. Jung, J. Shen, Y. Liu, J. M. Woods, Y. Sun, J. J. Cha, *Nano Lett.* **2014**, *14*, 6842.
[41] A. F. Mayadas, M. Shatzkes, J. F. Janak, *Appl. Phys. Lett.* **1969**, *14*, 345.
[42] M. Wei-Gang, W. Hai-Dong, Z. Xing, T. Koji, *Chin. Phys. B* **2009**, *18*, 2035.
[43] M. Yan, E. Wang, X. Zhou, G. Zhang, H. Zhang, K. Zhang, W. Yao, N. Lu, S. Yang, S. Wu, T. Yoshikawa, K. Miyamoto, T. Okuda, Y. Wu, P. Yu, W. Duan, S. Zhou, *2D Mater.* **2017**, *4*, 045015.
[44] B. M. Szydłowska, O. Hartwig, B. Tywoniuk, T. Hartman, T. Stimpel-Lindner, Z. Sofer, N. McEvoy, G. S. Duesberg, C. Backes, *2D Mater.* **2020**, *7*, 045027.
[45] R. Kempt, A. Kuc, T. Heine, *Angew. Chem., Int. Ed.* **2020**, *59*, 9242.
[46] L. Banszerus, H. Janssen, M. Otto, A. Epping, T. Taniguchi, K. Watanabe, B. Beschoten, D. Neumaier, C. Stampfer, *2D Mater.* **2017**, *4*, 025030.
[47] C. Neumann, S. Reichardt, P. Venezuela, M. Drögeler, L. Banszerus, M. Schmitz, K. Watanabe, T. Taniguchi, F. Mauri, B. Beschoten, S. V. Rotkin, C. Stampfer, *Nat. Commun.* **2015**, *6*, 8429.
[48] M. Belete, O. Engström, S. Vaziri, G. Lippert, M. Lukosius, S. Kataria, M. C. Lemme, *ACS Appl. Mater. Interfaces* 9656, **2020**, *12*.
[49] E. Okogbue, S. S. Han, T.-J. Ko, H.-S. Chung, J. Ma, M. S. Shawkat, J. H. Kim, J. H. Kim, E. Ji, K. H. Oh, L. Zhai, G.-H. Lee, Y. Jung, *Nano Lett.* **2019**, *19*, 7598.
[50] "GenISys ProSEM," can be found under https://prosem.genisys-gmbh.com/ (accessed: February 2021).
[51] M. Shaygan, M. Otto, A. A. Sagade, C. A. Chavarin, G. Bacher, W. Mertin, D. Neumaier, *Ann. Phys.* **2017**, *529*, 1600410.
[52] V. Podzorov, M. E. Gershenson, Ch. Kloc, R. Zeis, E. Bucher, *Appl. Phys. Lett.* **2004**, *84*, 3301.
[53] S. Vaziri, M. Ostling, M. C. Lemme, *ECS Trans.* **2011**, *41*, 165.
[54] N. R. Pradhan, D. Rhodes, Q. Zhang, S. Talapatra, M. Terrones, P. M. Ajayan, L. Balicas, *Appl. Phys. Lett.* **2013**, *102*, 123105.
[55] W. Bao, X. Cai, D. Kim, K. Sridhara, M. S. Fuhrer, *Appl. Phys. Lett.* **2013**, *102*, 042104.
[56] G. Nazir, M. F. Khan, V. M. Iermolenko, J. Eom, *RSC Adv.* **2016**, *6*, 60787.
[57] X. Jing, Y. Illarionov, E. Yalon, P. Zhou, T. Grasser, Y. Shi, M. Lanza, *Adv. Funct. Mater.* **2020**, *30*, 1901971.
[58] H. Zhong, Z. Zhang, H. Xu, C. Qiu, L.-M. Peng, *AIP Adv.* **2015**, *5*, 057136.
[59] T. Harriehausen, D. Schwarzenau, in *Moeller GrundlagenElektrotechnik* (Eds: T. Harriehausen, D. Schwarzenau), Springer Fachmedien, Wiesbaden **2020**, p. 27.
[60] S. P. Venkateshan, in *Mechanical Measurements*, John Wiley & Sons Ltd, Hoboken **2015**, pp. 243–279.
[61] A. S. Fiorillo, C. D. Critello, S. A. Pullano, *Sens. Actuators, A* **2018**, *281*, 156.
[62] J. Ruhkopf, S. Sawallich, M. Nagel, M. Otto, U. Plachetka, T. Kremers, U. Schnakenberg, S. Kataria, M. C. Lemme, *ACS Appl. Electron. Mater.* **2019**, *1*, 1909.
[63] S. Lukas, S. Kataria, M. Prechtl, O. Hartwig, A. Meledin, J. Mayer, D. Neumaier, G. S. Duesberg, M. C. Lemme, in *2020 Device Research Conf. (DRC)*, IEEE, Piscataway, NJ **2020**, pp. 1–2.
[64] A. Kovács, R. Schierholz, K. Tillmann, *J. Large-Scale Res. Facil. JLSRF* **2016**, *2*, 43.
[65] J. Heremans, *J. Phys. D: Appl. Phys.* **1993**, *26*, 1149.
[66] R. S. Popovic, J. A. Flanagan, P. A. Besse, *Sens. Actuators, A* **1996**, *56*, 39.